Electronic Supplementary Information

# Observing dynamic molecular changes at single-molecule level in a cucurbituril based plasmonic molecular junction

Qiushuang Ai, Jianghao Zhou, Jing Guo, Popular Pandey, Simin Liu, Qiang Fu, Yichong Liu, Chengji Deng, Shuai Chang*, Feng Liang*, Jin He*

**CONTENTS (Page S1)**

**S1. Chemicals (Page S2)**

**S2. Confirmation of the modification of CB[7] and its complexes on flat gold substrates by electrochemical and FTIR measurements (Page S2-S3)**

**S3. GNE fabrication, modification and characterization (Page S4)**

**S4. FDTD calculations (Page S5)**

**S5. Detailed spectral changes of a blinking event during an GNP collision event on CB[7] modified GNE (Page S5)**

**S6. DFT calculations (Page S6-S10)**

**S7. The assignment of vibrational peaks for the spectra of CB[7] molecule (Page S10-S11)**

**S8. The SERS spectra of citrate groups on the GNP (Page S11-S12)**

**S9. SERS spectra showing the C=O peak of CB[7] without the presence of citrate groups (Page S12)**

**S10. Stable C=O peak of CB[7] junctions after removing GNPs from the solution (Page S13)**

**S11. The SERS spectra showing C=O peak of FC@CB[7] (Page S13)**

**S12. Video of C=O vibration modes (Page S13)**

**S13. Electrochemical current measurements (Page S13-S14)**

**S14. 2D correlation and PCA analysis (Page S14-S15)**

## S1. Chemicals

Cucurbit[7]uril (CB[7]) was synthesized following a procedure published by Day□s group[1] and its purity is verified using $^1$H NMR (Fig. S1). Aminoferrocene (AFC) was purchased from TCL AMERICA (Portland, USA). Ferrocene (FC) and dopamine hydrochloride were purchased from Alfa Aesar (USA). Amantadine hydrochloride, potassium phosphate monobasic and potassium phosphate dibasic were purchased from Sigma-Aldrich (Saint Louis, USA). Phosphate buffered saline (PBS) powder (pH 7.3-7.5) and absolute ethanol (200 proof) were purchased from Fisher Scientific (USA). Potassium ferrocyanide (98.5% purity, analysis grade) was purchased from Acros Organics (New Jersey, USA). Citrate stabilized 40 nm diameter gold nanoparticles (GNPs) were purchased from Ted Pella, *Inc*.. All the purchased chemicals were used directly without further purification. All the aqueous solutions were prepared using deionized (DI) water (~18 M ohm, Purelab system, ELGA/Siemens).

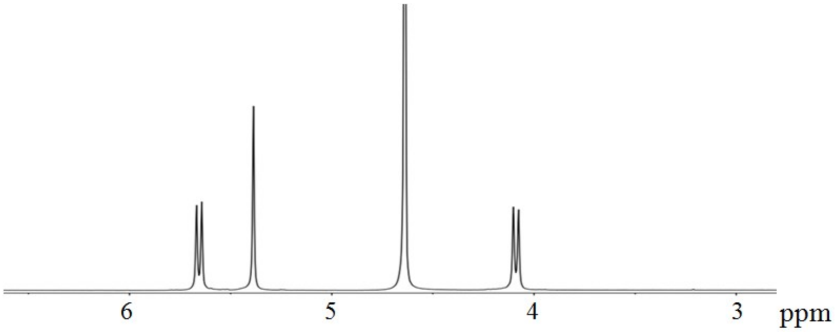

**Fig. S1. $^1$H NMR spectrum (600 MHz, $D_2O$) of CB[7].** (δ 5.63 (d, J = 15.3 Hz, 1H), 5.36 (s, 1H), 4.06 (d, J = 15.3 Hz, 1H)).

A 0.5 mM CB[7] solution was prepared by dissolving CB[7] powders in DI water with sonication for 5 mins. A 0.5 mM AFC@CB[7] molecule complex solution was prepared by mixing the AFC powder in the CB[7] solution (1:1 stoichiometry), followed by ~20 min sonication.

## S2. Confirmation of the modification of CB[7] and its complexes on flat gold substrates by electrochemical and FTIR measurements

### S2.1 Electrochemical measurements

Electrochemical measurements were carried out on macroscopic flat gold substrates to verify the successful complexation and modification of CB[7] and its complexes to the gold surface. Fig. S2.1a shows the cyclic voltammograms (CVs) of bare (black curve) and CB[7] functionalized (red curve) planar gold electrodes. No Faraday current were observed, showing that gold surface and CB[7] molecules are electrochemically inert in this potential range. When the electrode is modified with AFC@CB[7], the redox peak of AFC at ~0.21V is clear, indicating that the complexed AFC@CB[7] is successfully modified onto the gold surface. Similar observations are found in the electrochemical measurements of gold electrodes with FC@CB[7], as shown in Fig. S2.1b. By comparing the CVs of FC@CB[7] and AFC@CB[7], the redox peak of AFC@CB[7] is higher, suggesting the surface concentration of AFC@CB[7] is higher.

Fig. S2.1c and d show the CVs of gold electrodes before (black curve) and after (red curve) the immersion of the gold electrodes in 0.5 mM AFC or FC solutions (acetonitrile) for overnight. A small redox peak of AFC appears at ~0.23 V, suggesting the adsorption of AFC on the gold surface. However, this redox peak is not as distinct as that seen in the case of AFC@CB[7] modified gold surface (Fig. S2a). Therefore, more AFC molecules can be immobilized to the gold surface when they are encapsulated in CB[7]. In contrast, the redox peak of FC is not distinguishable in the CV (red curve of Fig. S2.1d) of FC modified gold electrode. This again suggests the AFC-gold interaction is stronger than the FC-gold interaction. If not encapsulated in the CB[7], few AFC or FC molecules can stay at the gold surface.

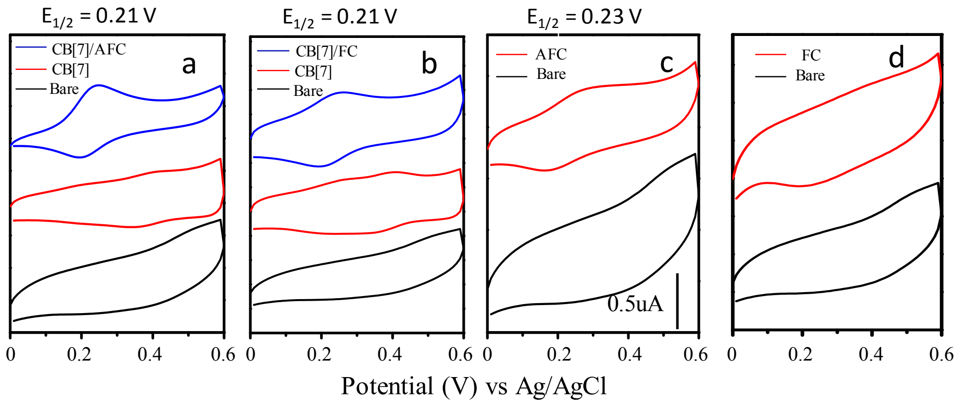

**Fig. S2.1. Cyclic voltammograms of molecules on planar gold electrodes. (**a) The CVs of bare (black curve), CB[7] (red curve) and AFC@CB[7] (blue curve) modified gold electrodes. (b) The CVs of bare (black curve), CB[7] (red curve) and FC@CB[7] (blue curve) modified gold electrodes before (black curve) and after the modification (red curve) of AFC (c) and FC (d). All the CVs were taken in 0.1 M $Na_2SO_4$.

## S2.2 FTIR characterization

The Fourier transfer infrared (FTIR) measurements were carried out for both CB[7] powders and the immobilized CB[7] molecules on a flat gold substrate. The results are summarized in Fig. S2.2. The details of all the peaks are listed in Table S3. It is interesting to note that most of the peaks shifted to the higher wavenumber after the adsorption of CB[7] to the gold substrate (see section S7). This is consistent with the red-shifts observed in Raman spectra. The red color spectrum in Fig. S2.2 is the DFT calculated CB[7] IR spectrum (see section S6 for the DFT calculation). The peaks are matched reasonably well.

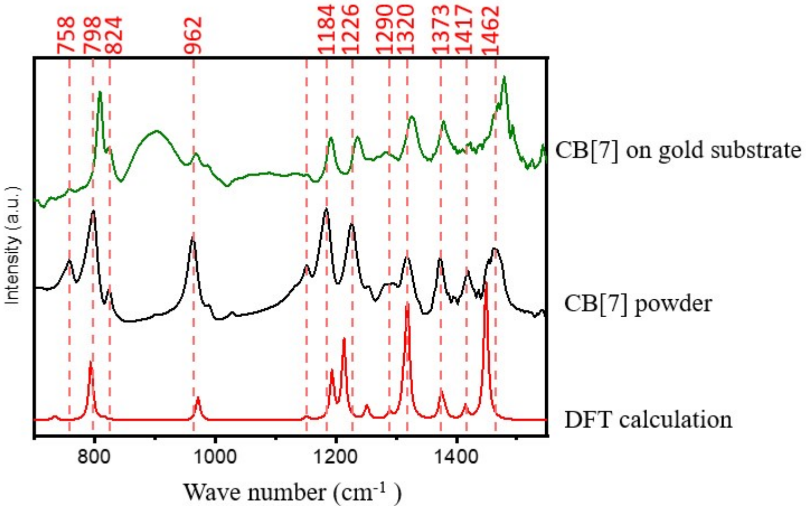

**Fig. S2.2. IR spectra of CB[7].** The spectra of FTIR measurements of CB[7] powder (black) and CB[7] functionalized gold substrates (green). The DFT calculated IR spectrum is shown at the bottom for comparison (red).

## S3. GNE fabrication, modification and characterization

The details of the GNE fabrication has been described elsewhere.[2, 3] In brief, the GNE was prepared from a 0.2 mm diameter gold wire (Electron Microscopy Sciences, 99.99%) *via* an electrochemical etching method. The etched GNE has a typical apex radius of ~300 nm, as shown in Fig. S3a. After cleaning, the GNE was partially insulated with a high-density polyethylene (HDPE) coating. To achieve the partial insulation, the GNE tip was slowly driven through a drop of melted HDPE. When the GNE tip came out of the melted HDPE drop, the HDPE layer coated over the GNE apex cooled off and shrank, leaving the apex exposed.

For chemical modification, the insulated GNE was immersed in the molecule solution for at least 12-14 hours at room temperature. Subsequently, the GNE was rinsed with DI water. The successful modification of CB[7] on GNE is confirmed by means of both scanning electron microscope (SEM) and cyclic voltammetry (CV). Two GNEs, with and without CB[7] modification (both were not insulated), were immersed in a 30 pM GNP (40 nm diameter) solution for 2 hours. After rinsing, they were imaged by SEM. No GNPs appear at the surface of bare GNE apex (Fig. S3a). In contrast, in Fig. S3b, several GNPs appear at the CB[7] modified GNE apex, indicating the successful modification of GNE with CB[7]. The SEM image of a large quantity of 40 nm GNPs is shown in Fig.S3c. Because of charging, the GNPs appear slightly bigger than the mean size about 41 nm characterized by the company Ted Pella using TEM. The CV was carried out in 1M KCl solution with 100 mM ferrocyanide ion. The potential sweep rate was 10 mV/s. As shown in Fig. S3d, after the CB[7] modification, the electrochemical current is reduced.

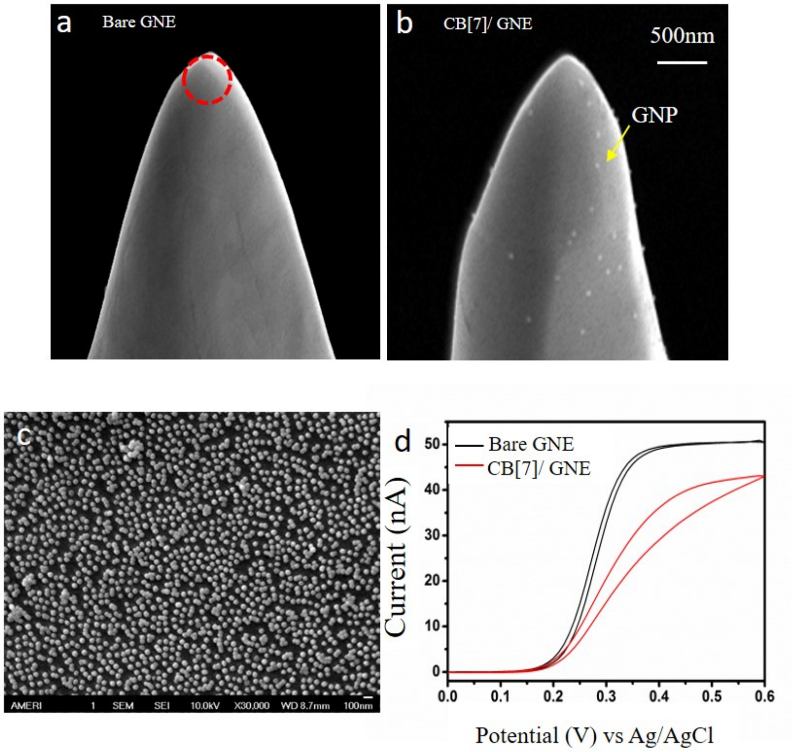

**Fig. S3. SEM images and CVs of the GNE.** (a-c) SEM images of a bare GNE (a) and a CB[7] modified GNE with adsorbed GNPs (b) after immersion of 2 hours in a GNP solution. (c) The GNPs on a glass substrate. The red dashed line circle in (a) indicates a tip radius of ~300 nm. (d) The CVs of a GNE before (black curve) and after CB[7] (red curve) modification.

## S4. FDTD calculations

### S4.1. The setup of FDTD simulation

The 3D-FDTD simulation was performed by a commercial software package (Lumerical Solutions Inc.). The modeled NPoNE nanogap junction is illustrated in Fig. S4a, a gold sphere with radius $R_1$ (20 nm) on a gold hemisphere with radius $R_2$ (300 nm). As shown in Fig. S4b, the gap distance between the two surfaces is fixed at 0.91 nm, which is based on the height of CB[7]. For comparison, we also replaced the bottom hemisphere with a flat plane, representing the nanoparticle-on-mirror (NPoM) geometry.

In simulation, a TFSF (Total-field scattered-field) wave was used for the incident light with a wavelength $\lambda = 633$ nm. The polarization direction is parallel to the nanogap center axis (Z direction). The Yee cell size used in the 3D-FDTD simulation was set to be 5 nm cube for the surroundings away from the nanogap and the gold surfaces, and $0.32 \times 0.32 \times 0.1$ nm in the nanogap. The number of layers for the perfect matching layer (PML) boundary was set to be 32 and the total simulation time was set to be 1000 fs, which ensures the calculation to converge properly. The refractive index of the surrounding media is 1 for vacuum.

### S4.2. Electric field amplitude distribution in the cross section of the nanogap

As shown in Fig. S4c, the normalized electric field amplitude ($|E/E_0|$, $|E_0|$ is the amplitude of incident light) in the center of the nanogap is more than 216, corresponding to a $10^9$ SERS signal enhancement. For comparison, the maximum $|E/E_0|$ at the center of a nanogap between a 40 nm diameter gold sphere and a flat plane is about 1.4 times smaller, leading to a ~3.8-time reduction in the SERS enhancement factor.

The $|E/E_0|$ distribution at the center of the nanogap in the x-y plane is shown in the logarithmic scale in Fig. S4c. The diameters for the regions with $10^9$, $10^8$, and $10^7$ SERS enhancement factor are 3.80 nm, 8.86 nm and 12.66 nm, respectively.

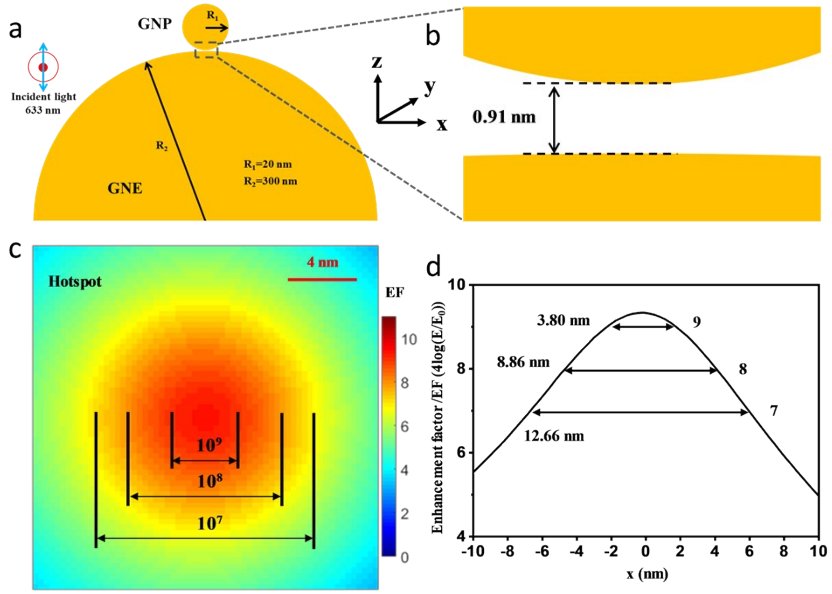

**Fig. S4. The electric field enhancement distribution.** (a) The modeled nanogap structure of the NPoNE. The $R_1$ of GNP is fixed at 20 nm and the $R_2$ of GNE is 300 nm. The direction of incident laser ($\lambda$=633 nm) is in y direction and is perpendicular to the paper plane (x-z) and the E-field of the laser is parallel to the z axis of the nanogap. (b) The zoom-in of the nanogap geometry. (c) The Raman enhancement factor $E_F$ ($=|E/E_0|^4$) in logarithmic scale distribution in the x-y plane inside the nanogap. (d) The $E_F$ distribution in logarithmic scale along the x axis where y, z = 0. The origin of the coordinate system is at the center of the nanogap.

## S5. Detailed spectral changes of a blinking event during an GNP collision event on CB[7] modified GNE

The progressive spectra are displayed in time series (51.9 ms interval) from bottom to up, with the bottom black color spectrum occurring at 60.3 s. They are from a longer lifetime event near 60.3 s in the SERS trajectory in Fig. 2a of main text.

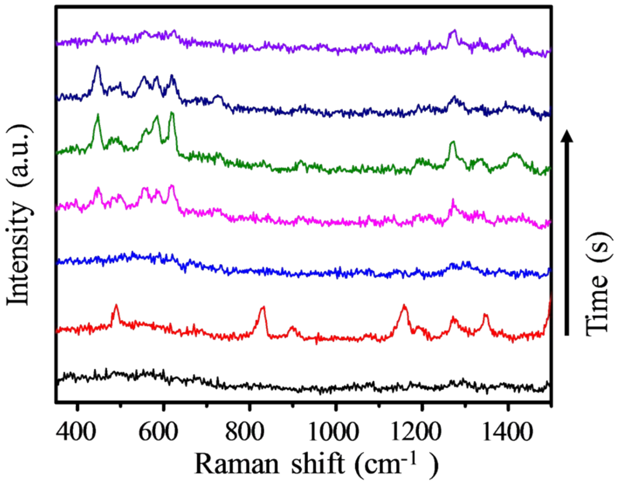

**Fig. S5. Progressive SERS spectra of a blinking event with a longer lifetime.** Each spectrum takes 51.9 ms.

## S6. DFT calculations

### General

We have calculated the vibrational spectra using both B3LYP and Coulomb-attenuating method (CAM)-B3LYP hybrid exchange□correlation functionals. We used 6-31G** basis set for molecule and LANL2DZ basis set for gold atoms. The calculated Raman spectra of AFC and FC with and without CAM are shown in Fig. S6.1a. The Raman spectra calculated with both functionals are very similar. The main difference is that the calculated spectra using CAM-B3LYP is multiplied by a smaller scaling factor. Similar conclusions can be drawn for CB[7] (Fig. S6.1b). The Raman spectra of CB[7] using CAM-B3LYP can fit slightly better with the experimental results (especially at the lower wavenumber). The details can be found in Table S1. We therefore used CAM-B3LYP for most of the calculations.

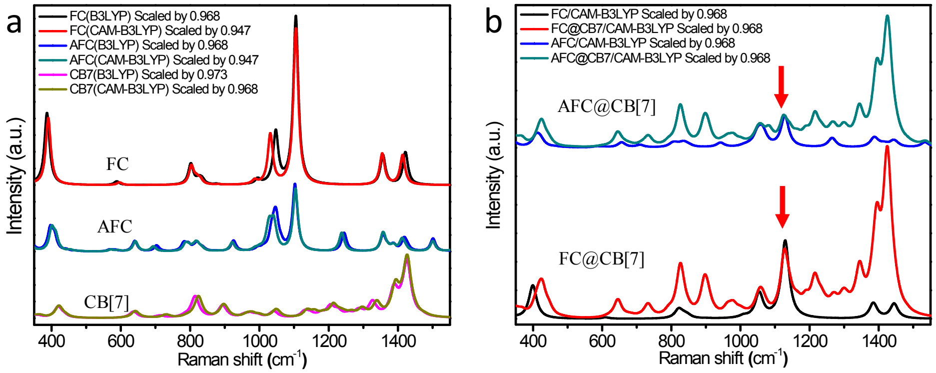

**Fig. S6.1. Calculated Raman spectra of CB[7] and its host-guest complexes. (**a) Raman spectra of FC, AFC and CB[7] using B3LYP and CAM-B3LYP functionals. (b) Raman spectra of CB[7] and CB[7]@FC/CB[7]@AFC using CAM-B3LYP functionals. The FC and AFC spectra are also shown for comparison.

**Table S1. The peak position comparison of the spectra of CB[7], FC@CB[7], and AFC@CB[7]**

| Wavenumber (cm$^{-1}$) | a | b | c | d | e | f | g |
|---|---|---|---|---|---|---|---|
| CB[7](B3LYP) | 419 | 814 | 893 | 1206 | 1326 | 1389 | 1425 |
| CB[7](CAM-B3LYP) | 421 | 824 | 897 | 1214 | 1339 | 1394 | 1426 |
| FC@CB[7](CAM-B3LYP) | 420 | 812 | 888 | 1199 | 1322 | 1385 | 1423 |
| AFC@CB[7](CAM-B3LYP) | 421 | 813 | 888 | 1199 | 1322 | 1386 | 1423 |

**The C=O peak**

We summarized the experimental peak position of ν (C=O) mode appeared in stable junctions of CB[7], FC@CB[7] and AFC@CB[7]. For CB[7], the junction is obviously more stable at 0.5 V. Therefore, we compared all the experimental results at 0.5 V. Fig. S6.2a shows the distributions of C=O peak position appeared in experiments for three molecules. The most frequent C=O peak position is 2170 cm$^{-1}$ for CB[7], 2150 cm$^{-1}$ for FC@CB[7] (also see Fig. S11) and 2120 cm$^{-1}$ for AFC@CB[7].

To understand the mechanism for the spectral shift of the C=O peak, we also compared the C=O peak position in the DFT calculated spectra of CB[7], FC@CB[7] and AFC@CB[7]. We first checked the vibration modes of C=O for the CB[7]. Two C=O peaks can be found in the DFT calculated spectrum, as shown as the black color spectrum in Fig. S6.2b. The major peak (with a higher wavenumber) of CB[7] is due to the synchronized symmetric vibration of all the carbonyl groups. In this mode, the symmetric vibrations of carbonyl groups in 7 glycoluril units happen at the same time. The minor peak is due to the asynchronized symmetric vibration (see video file SM1). In this mode, the symmetric vibrations of carbonyl groups in 7 glycoluril units do not happen at the same time and is out of phase. We will focus on the major C=O peak in the following discussions. As shown in Fig. S6.2b, there is a small red shift of the major C=O peak from CB[7] to FC@CB[7] and AFC@CB[7], which is consistent with the trend observed in the experimental result.

To investigate the reason of this red shift, we have analyzed the charge distribution of the three molecular systems. When FC or AFC is added into the CB[7] cavity, the electron cloud of CB[7] slightly shifts from the carbonyls of CB[7] to the Cp rings of FC or AFC, resulting a reduced electron density in the C=O groups. Therefore, the wavenumber of C=O peak is reduced. In addition, for AFC, the amine group also induces the electron cloud to shift away from the carbonyls. Therefore, the wavenumber of *v*(C=O) mode peak of AFC@CB[7] complex is even lower than that in the FC@CB[7] complex.

The red shifts in the experimental results are much bigger than the calculated results. One obvious reason for the discrepancy is attributed to the charge transfer between the carbonyl groups of CB[7] and gold electrodes, which are not included in the DFT calculations here.

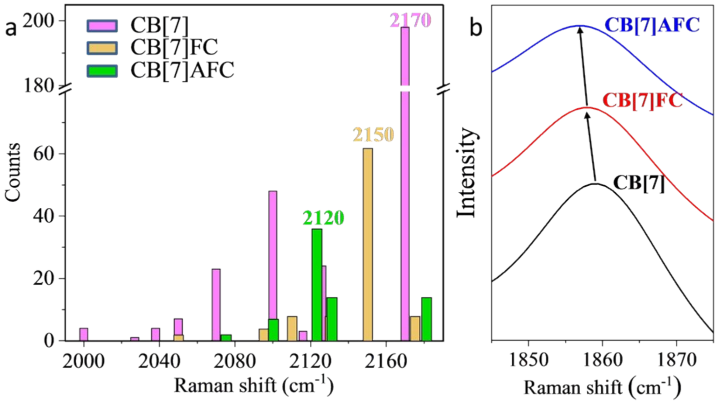

**Fig S6.2. The stable C=O peak position.** (a) Experimental results for the distributions of stable C=O peak position of CB[7] and its host-guest complexes at 0.5 V. (b) Calculated *v*(C=O) mode peaks of CB[7] and its host-guest complexes. The arrow indicates the red shift of the major C=O peak.

### The Au4-glycoluril-Au4 system

To better understand the spectral shift of the C=O peak in the NPoPE geometry, we added gold clusters into the model structures for DFT calculation. In order to reduce the calculation cost, we chose the Au4 cluster to represent the GNE and GNP. The Au4 cluster is typically used in DFT calculation and its size is suitable for glycoluril. We carried out calculations using three types of model structures, which are glycoluril only, glycoluril with one Au4 cluster, and glycoluril sandwiched between two Au4 clusters. The structures of the last two types are shown in Fig. 3a.

In the calculated Raman spectra (Fig. 3b), two C=O peaks can be observed. We assigned the two peaks to the symmetric and asymmetric vibration modes of two carbonyl groups. The symmetric vibration mode (the major peak at the higher wavenumber) is the stretching of two carbonyl groups in the opposite direction and the asymmetric vibration mode is the stretching of two carbonyl groups in the same direction. The two C=O vibration modes of glycoluril and the symmetric C=O vibration mode in Au4-1/glycoluril/Au4-2 structures are shown in the video file SM2.

### The Au20-FC-Au20 and Au20-AFC-Au20 systems

The Raman spectra of FC@CB[7] and AFC@CB[7] host-guest complex results are shown in Fig. S6.1b. To investigate the charge transfer between FC/AFC and gold clusters, we further included the bigger Au20 cluster structures in DFT calculations. In this section, we used PW91PW91 functional, which can better calculate the metal-molecule charge transfer effect. Basis sets 6-311+g(d, p), 6-311g(2df) and LANL2DZ were used for C, H, O atoms, Fe atom and gold atoms, respectively. A scale factor very close to 1 (0.996) was used for the calculated spectra. For the Au20 cluster, the gold atoms have different reactivity and the ones at the four apexes have the highest reactivity. The FC and AFC molecules may also orient differently on the gold surface while confined in the CB[7] cavity. Therefore, we have calculated total 8 different metal-molecule-metal systems as shown in Fig. S6.3a. All the structures reached the minimized energy. The nanogap distance varied slightly in the energy minimization process and the exact distances are listed. The calculated Raman peaks of Cp breathing mode are shown in Fig. S6.3b. The spectra of FC and AFC were also recalculated using the same functional and basis sets for comparison. The largest down-shift of the Cp breathing mode peak is to 1080 cm$^{-1}$ for structures 6 and 7. The structure 2 show two peaks, attributing to the different interactions between the Au20 tip-Cp ring center and Au20 base-Cp ring center.

It should be noted that the accuracy of the structures with FC and AFC at the horizontal orientation is lower than the vertical cases. The interaction between Au20 cluster and the FC or AFC in the horizontal orientation is much weaker. So the complex is difficult to form in the DFT calculation. This is reasonable because the horizontal orientation is mainly stabilized by the CB[7] cavity in experiment. During the energy minimization process, the molecule tends to move closer to the gold than the actual case in order to form a stable complex. Especially, the FC and AFC in structures 1, 5 and 8 are deformed in the energy minimization process of Gaussian. Therefore, we manually determined the energy-minimized structures by calculating a series of structures at various distances while fixing the molecular structures of FC and AFC.

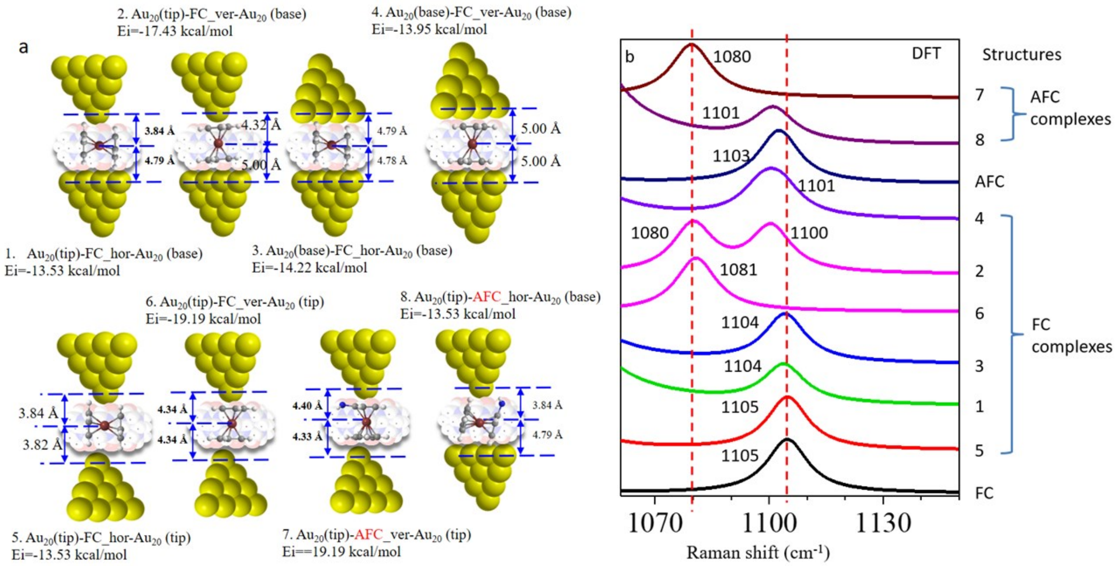

**Fig. S6.3.** (a) The calculated 8 configurations of Au20-FC-Au20 and Au20-AFC-Au20 complexes. (b) The corresponding Raman spectra for the Cp breathing mode.

We also calculated the interaction energy ($E_i$) between the FC/AFC molecule and the Au20 cluster by using the equation $E_i = E_{complex}-E_{molecule}-E_{Au20}$. Eight structures are shown below in Fig. S6.4. The interaction energy and the distances between the top gold atom and the iron center of the molecule are also shown in the Fig. S6.4. All structures were calculated by energy minimization except structures (iii) and (vii). For the structures (iii) and (vii), the FC and AFC were deformed after energy minimization. We therefore optimized the structures of FC/AFC and Au20 separately and then placed them together at various distances to find the energy minimized structure. For structures (iv) and (viii), as we explained in the previous paragraph, we expect the actual distance is slightly bigger and the interaction energy is slightly smaller. Overall, the strongest interaction is between the Cp ring center and the Au20 tip ((i) for FC and (v) and (vi) for AFC). Between FC (structure (i)) and AFC (structures (v) and (vi)), the Cp ring center of AFC has a bigger interaction energy with the Au20 tip. The interaction between Cp ring center with the Au20 base is weaker (see (ii)). When the FC is in the horizontal orientation, the interactions between Cp ring edge or iron center with either Au20 tip or Au20 base are also weak. The binding energy $E_i$ ($=E_{complex}-E_{molecule}-2E_{Au20}$) for 8 Au20-molecule-Au20 structures are also listed in Fig. S6.3a.

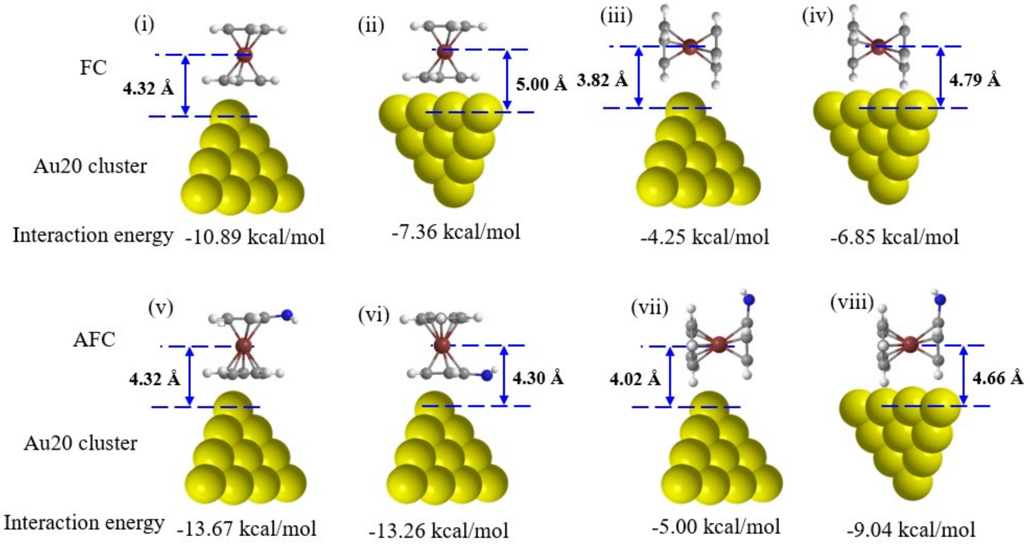

**Fig. S6.4. The calculated 8 structures of molecule-Au20 complex for interaction energy ($E_i$).** Top panel, FC; Bottom panel, AFC.

We also investigated the charge transfer in these structures. Table S2 gives the partial charge values of every component of these structures. For comparison, the charge distributions in FC and AFC also listed in Table S2. All structures are neutral and the total net charge is zero. The negative value means the component gains electron and the positive value means the component loses electron. As expected, the molecule-metal electron transfer is very sensitive to the details of molecule-metal interactions. As expected, the electronic coupling is strongest between the Cp ring center and the Au20 tip, which has the highest reactivity. The electron is withdrawn from the Cp ring to Au20 tip. In contrast, the amount of charge transferred between the Cp ring center and Au20 base is very small and the direction is opposite. Similar results are observed for the charge transfer between the Cp ring edge and the Au20 tip or base. Because of the effective electron transfer from the Cp ring center to the Au20 tip, the peak of breathing vibration in Cp ring is obviously shifted to the lower wavenumber (red shift) from 1105 to 1080 $cm^{-1}$.

**Table S2. The calculated Mulliken partial charge (unit: e=1.6 × $10^{-19}$ C) at each component of the structures.**

| | Au20-NP | $Cp_1$ | Fe | $Cp_2$ | Au20-NE |
|---|---|---|---|---|---|
| FC only | N/A | -0.565 | 1.31 | -0.565 | N/A |
| AFC only | N/A | -0.603(amine: 0.102) | 1.01 | -0.603 | N/A |
| 1. Au20(tip)-FC_hor-Au20 (base) | -0.227 | -0.303 | 1.169 | -0.699 | 0.064 |
| 2. Au20(tip)-FC_ver-Au20 (base) | -0.497 | -0.219 | 1.23 | -0.322 | -0.196 |
| 3. Au20(base)_FC_hor_Au20 (base) | 0.056 | -0.594 | 1.081 | -0.595 | 0.053 |
| 4. Au20(base)_FC_ver_Au20 (base) | 0.128 | -0.902 | 1.531 | -0.806 | 0.052 |

| | | | | | |
|---|---|---|---|---|---|
| 5. Au20(tip)_FC_hor_Au20 (base) | 0.056 | -0.594 | 1.081 | -0.595 | 0.053 |
| 6. Au20(tip)_FC_ver_Au20 (tip) | -0.475 | -0.031 | 0.876 | -0.039 | -0.473 |
| 7. Au20(tip)_AFC_ver_Au20(tip) | -0.454 | -0.148 (amine: 0.164) | 0.955 | -0.119 | -0.396 |
| 8. Au20(tip)_AFC_hor_Au20(base) | -0.166 | -0.525 (amine: 0.189) | 1.135 | -0.488 | -0.144 |

Note 1: the total charge on each structure is zero.

## S7 The assignment of vibrational peaks for the spectra of CB[7] molecule

### S7.1 Raman spectrum of CB[7] powder

Fig. S7 shows the measured Raman spectrum of CB[7] powders on the cover glass. The DFT calculated Raman spectrum (blue curve) is shown at the bottom for comparison. The peaks are matched reasonably well. The six of the major fingerprint vibrational modes at 436, 656, 831, 913, 1383 and 1417 cm$^{-1}$ are indicated.

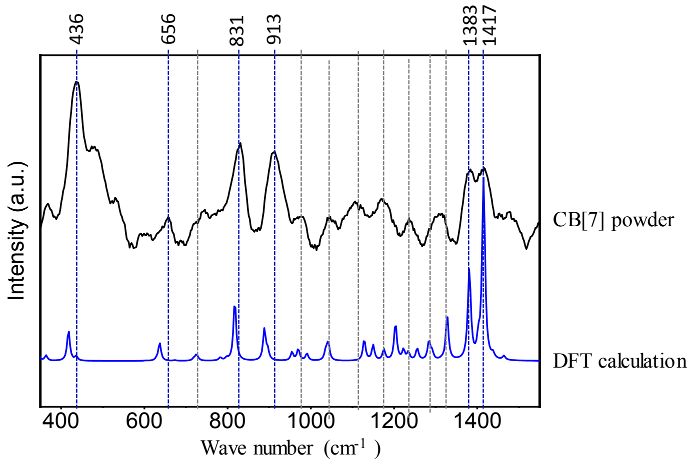

**Fig. S7. The Raman spectrum of CB[7] powder.** The Raman spectrum is recorded with 1.5 s exposure time by laser 633 nm**.**

Based on the experimental and theoretical works, we assigned the peaks as listed in Table S3.

**Table S3. Assignments of vibrational peaks for CB[7]**

| IR | | | Raman | | | Assignments [a, b] |
|---|---|---|---|---|---|---|
| Calculated | Powder | On gold | Calculated | Powder | SERS | |
| | - | - | 420 (s) | 436 (s) | 440 | σN-C-N |
| | - | - | 641 (m) | 656 (m) | 657 (m) | τ HC-CH |
| 793(s) | 796 (s) | 810 (s) | 817 (s) | 831 (s) | 808 | δ C-N-C + ρCH2 |
| | - | - | 889 (s) | 913 (s) | 901 | βC-N-C + τ N-C-C-N+ ν C-C |
| 972 (m) | 962 (s) | 968 (m) | 954, 967, 992 (w) | 977(overlap, w) | - | ν HC-CH+ δ N-C-N |
| | - | - | 1041 (w) | 1042 (w) | 1063 | ν HC-CH+ δ N-C-N |

| | | | | | | |
|---|---|---|---|---|---|---|
| 1193 (s) | 1184 (s) | 1192 (s) | 1127, 1150, 1176 (w) | 1106, 1171 | 1150 | σ HC-CH + ν C-C |
| 1213 (s) | 1226 (s) | 1236 (s) | 1204 (m) | - | - | σ N-C-N + ρ HC-CH+σ C-C |
| 1250 (w) | 1254 (w) | - | 1222, 1234, 1254 (w) | 1236 | 1240 | ρ CH |
| 1288 (w) | 1280 (w) | - | 1285 (w) | overlapped with 1316 | 1288 | ν N-C-N + ρ HC-CH |
| 1320 (s) | 1320 (s) | 1326 (s) | 1328 (w) | 1316 (m) | - | ν N-C-N + ν N-C-C-N |
| 1375 (w) | 1373 (s) | 1379 (s) | 1380 (s) | 1383 (s) | 1380 | Symmetric ν C-N |
| 1415 (w) | 1417 (m) | - | 1415 (s) | 1417 (s) | 1430 | Asymmetric ν C-N |
| 1450 (s) | 1462 (s) | 1479 (s) | - | - | - | ν C-N |

a The notations of the modes are: ν = stretch, τ = twist, σ = scissor, δ = deformation, ρ = rock, and β = bend[4].

b Follow the previous assignments [5, 6]

## S8. The SERS spectra of citrate groups on the GNP

We have carried out the control experiments to study the SERS signal generated by the collision events of citrate stabilized GNPs on bare GNE. These signals should all from the citrate groups on the GNP surface. Fig. S8a shows the typical time-dependent SERS spectra of citrate from the control experiments. Fig. S8b shows three spectra at different time points (indicated by the arrows in Fig. S8a). The citrate spectra are weak and highly dynamic. The strongest peak of the citrate spectra is always near 1546 cm$^{-1}$, which is also very broad. Some weak peaks are observed between 1988 cm$^{-1}$ and 2142 cm$^{-1}$. They are assigned to the ν(C=O) modes of citrate carbonyl groups and appear less frequently.

Because the SERS spectra of citrate are unstable, we analyzed the appearance of citrate peaks in the spectral range from 400 cm$^{-1}$ to 2300 cm$^{-1}$ in the dynamic events. An event was counted when more than one peak show sudden changes in the same time period. Examples of three events with longer lifetime are shown in Fig. S8a. We counted total 492 events. Fig. S8c shows the SERS peaks mainly appear near 1546.1 cm$^{-1}$ and less peaks appear at other spectral range. In the range between 1800 cm$^{-1}$ and 2300 cm$^{-1}$, the peaks mainly appear near 2142 cm$^{-1}$.

We calculated the intensity ratio between the ν(C=O) peak and the broad peak near 1546 cm$^{-1}$ when both peaks appear in the spectrum at the same time. The statistical result is shown in Fig. S8d. The mean value of the ratio is 0.32 and the maximum value is about 0.5. In contrast, the C=O peak of CB[7] usually much higher than other peaks in the spectra. Therefore, the C=O peak of citrate should only has a small contribution to the strong C=O peak appeared in the CB[7] experiments.

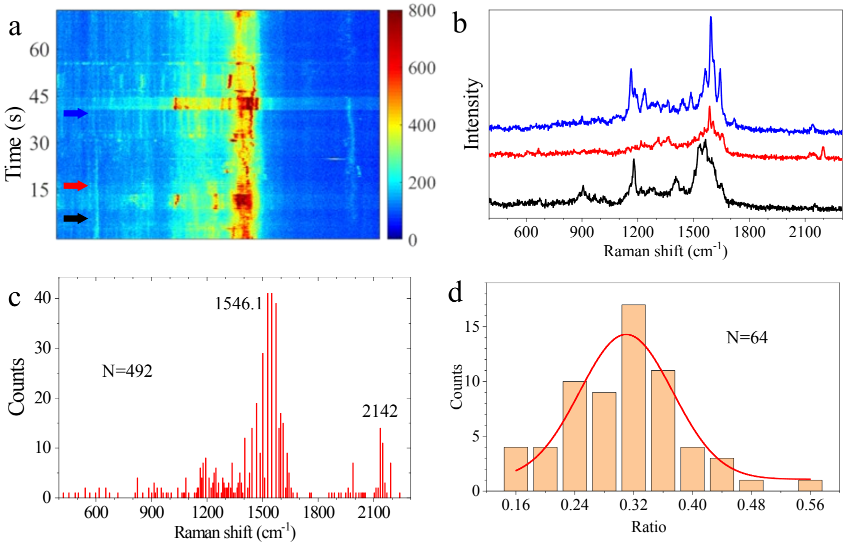

**Fig. S8. The analysis of the SERS spectra of citrate groups from the GNP.** (a) The typical SERS time trajectory of citrate stabilized GNP on the bare GNE. (b) There spectra from the time trajectory in (a). (c) The appearance of SERS peaks in the spectral range 400 cm$^{-1}$ to 2300 cm$^{-1}$ based on 492 events. (d) The distribution of intensity ratio of 1546 cm$^{-1}$ peak versus the *v*(C=O) peak in the range 1800 cm$^{-1}$-2300 cm$^{-1}$ from 64 events. The solid line is from the Gaussian fit.

## S9. SERS spectra showing the C=O peak of CB[7] without the presence of citrate groups

In order to further confirm that the strong peaks in the spectral range of 2000 cm$^{-1}$-2200 cm$^{-1}$ in the CB[7] experiments are from stretching of carbonyl groups of CB[7], we carried out another group of control experiments. We replaced the citrate groups on the GNP surface by 4-MBA molecules. With the adsorption of 4-MBA-GNPs to the cysteamine modified GNE or CB[7] and cysteamine modified GNE, we can form two types of junctions, GNE-cysteamine/4-MBA-GNP and GNE-CB[7](cysteamine)/4-MBA/GNP junctions. Here we introduce the cysteamine molecule to enhance the adsorption of GNPs to the GNE surface. The experimental results are shown in Fig. S9. In the time-dependent SERS spectra of GNE-CB[7](cysteamine)/4-MBA-GNP junction (Fig. S9a), the major peaks of 4-MBA peaks and cysteamine can be identified below 1600 cm$^{-1}$. In this range, the CB[7] peaks are very weak and cannot be clearly distinguished. However, we can observe a clear peak appear in the spectral range of 2100 cm$^{-1}$-2200 cm$^{-1}$. In contrast, in the GNE-cysteamine/MBA-GNP junction without CB[7], almost no peak appears in the same range at all. Fig. S9c shows the individual spectra taken from the trajectories in Fig. S9a and b. Because we already removed the citrate molecules from the GNP surface, the C=O peak in the range of 2100 cm$^{-1}$ to 2200 cm$^{-1}$ should come from the vibration of carbonyl of CB[7].

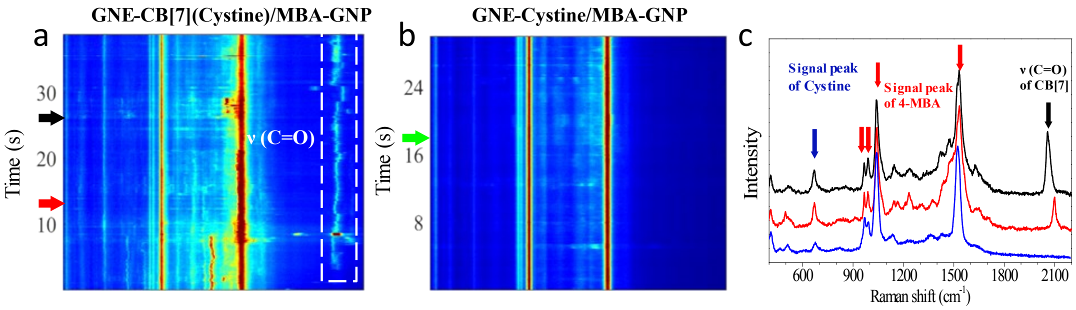

**Fig. S9. The SERS spectra showing the C=O peak of CB[7] without the presence of citrate groups.** (a) The typical SERS time trajectory taken from the GNE-CB[7](cysteamine)/4-MBA-GNP junctions. (b) The typical SERS time trajectory taken from the GNE-cysteamine/4-MBA-GNP junctions. (c) The individual spectra from the time trajectories in (a) and (b), indicated by the arrows.

## S10. Stable C=O peak of CB[7] junctions after removing GNPs from the solution

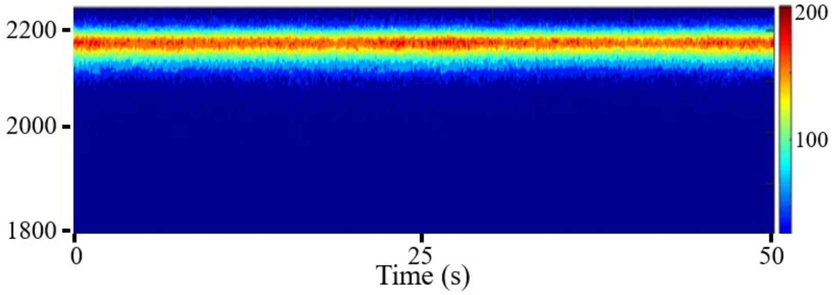

**Fig. S10. The stability of the C=O peak of CB[7] without the interference of free-moving GNPs in the solution.** The time-resolved SERS trajectory acquired from a CB[7] functionalized GNE in the absence of GNPs in the electrolyte solution. The applied bias is +0.5 V. The C=O peak near 2170 cm$^{-1}$ is quite stable.

## S11. The SERS spectra showing C=O peak of FC@CB[7]

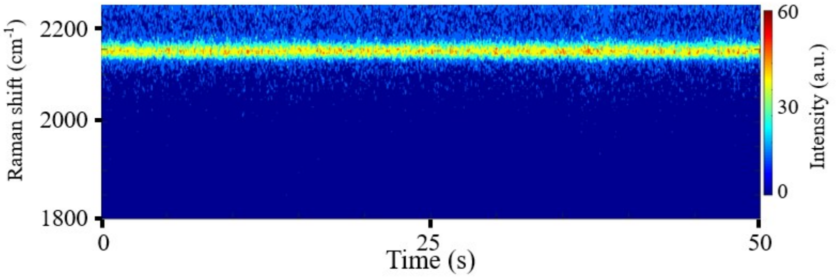

**Fig. S11. The SERS spectra of the C=O peak of FC@CB[7].** The time-resolved SERS trajectory acquired from a FC@CB[7] functionalized GNE. There is no applied bias. The C=O peak is near 2150 cm$^{-1}$. The spectrum was taken after adding GNP in the solution for 45 mins.

## S12. Video of C=O vibration modes

**Video 1. C=O vibration peaks of CB[7]**

**Video 2. Vibration modes of C=O peak of glycoluril**

## S13. Electrochemical current measurements

By setting the potential of the GNE at +0.5 V with respect to an Ag/AgCl reference electrode in electrolyte with redox mediator ($Fe(CN)_6^{4-}$), we recorded the electrochemical (EC) current through the GNE during the SERS measurements. Fig. S12 presents the typical EC current time traces of CB[7] functionalized GNEs with GNPs in solution. A number of upward current spikes are observed when the electrode potential is above 0.4 V. In addition, these current spikes only occur after the addition of GNPs in the electrolyte and are attributed to the transient stay of GNPs at the CB[7] modified GNE. Similar current spikes were observed in electrochemical measurements of nanoparticle collisions at molecule modified micro-/nano-sized electrodes.[2, 7] As shown in Table S4, The observed current spike in average is higher in magnitude and longer in duration time when AFC is inside the CB[7] cavity. In general, the event rate of current spikes is also higher for AFC@CB[7]. These results reflect the stronger interaction between GNPs and the AFC@CB[7] immobilized on the GNE.

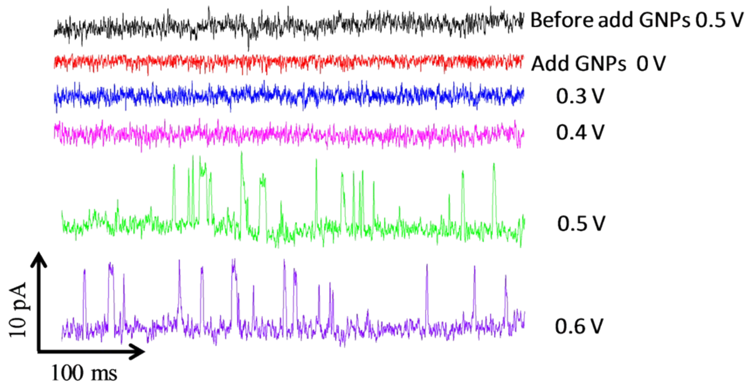

**Fig. S12.** Typical electrochemical current time traces for CB[7] at different applied potentials.

## Table S4. Statistical analysis of observed current spikes at 0.5 V

| | Spike amplitude (pA) | Spike duration (ms) |
|---|---|---|
| CB[7] | 3.8 ± 0.3 | 19.4 ± 1.4 |

| | | |
|---|---|---|
| FC@CB[7] | 4.9 ± 0.2 | 19.6 ± 0.7 |
| AFC@CB[7] | 6.9 ± 0.5 | 26.4 ± 1.6 |

## S14. 2D correlation and PCA analysis

We have carried out two-dimensional correlation spectroscopy (2D-COS) analysis and principal component analysis (PCA) of the time-resolved SERS results by using Origin software. The 2D correlation contour maps of CB[7] junction (Fig. 6a) and AFC@CB[7] junction (Fig. 6b) were constructed from blinking data of Fig.2a (about 266 frames) and Fig.4a (about 221 frames), respectively. The baselines of the spectra were corrected before the analysis.

The PCA results of the CB[7] and AFC@CB[7] data are shown in Fig.S13. The scree plots are shown in Fig. S13a and b. The first four principal components for CB[7] are PC1 33%, PC2 19.8%, PC3 10%, and PC4 5.6% respectively, and account for 68.4% cumulative variance as shown in Fig. S13a. For the AFC@CB[7], the first four PCs are PC1 (31.7%), PC2 (12.8%), PC3 (8.6%), and PC4 (6%), with a total 59.1% cumulative variation as shown in Fig. S13b. Due to the low value of PCs, the first four PCs were selected for further analysis. The PCA score plots were plotted with the first three PCs. The wide distribution of scores reflects the large variation of spectra generated from different collision events.

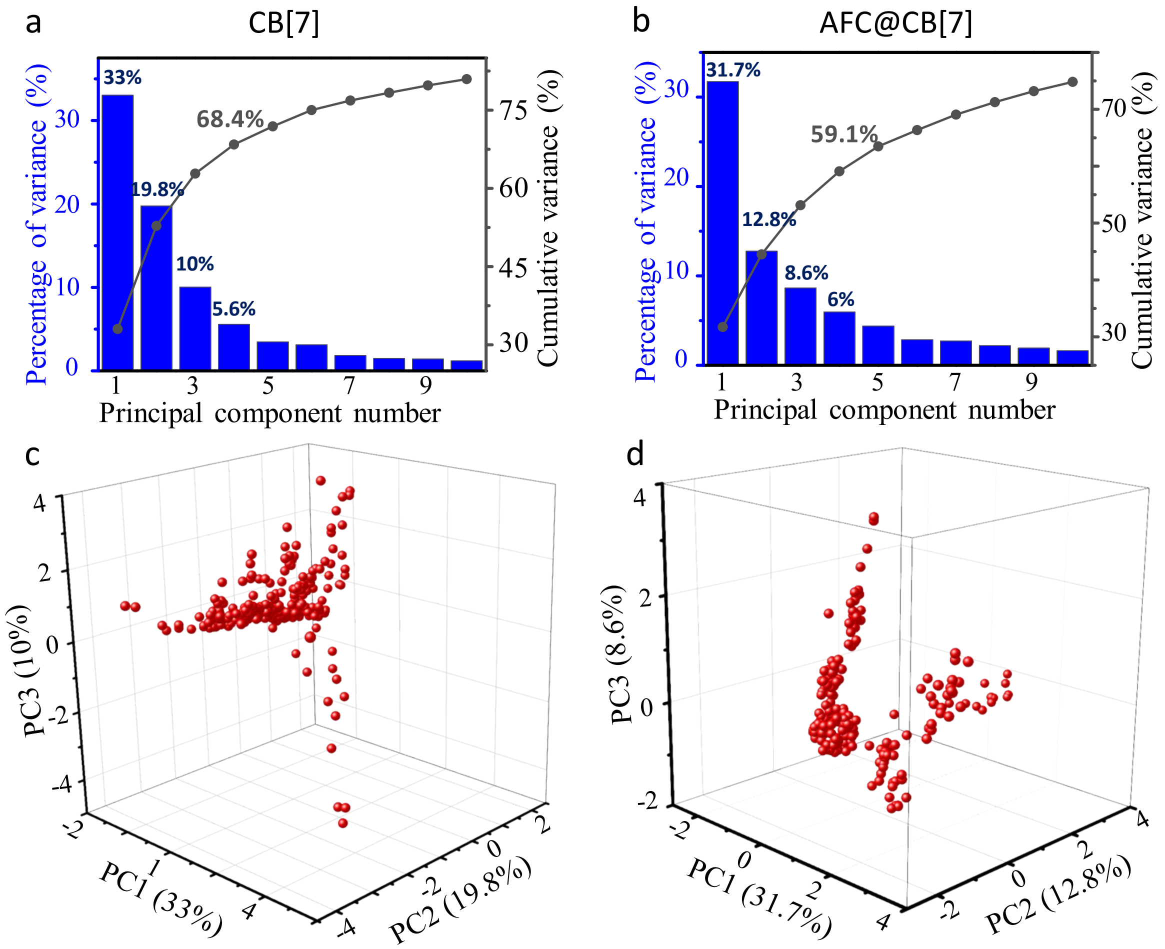

**Fig. S13. PCA for the time-resolved SERS data of CB[7] (data from Fig.2a) and AFC@CB[7] (data from Fig.4a).** (a-b) Scree plots of the principal components for CB[7] (a) and AFC@CB[7] (b). (c-d) 3D scatter plots of the scores for CB[7] (c) and AFC@CB[7] (d) under the first three PCs.

## References

1. A. Day, A. P. Arnold, R. J. Blanch and B. Snushall, *J. Org. Chem.*, 2001, **66**, 8094.
2. J. Guo, J. Pan, S. Chang, X. Wang, N. Kong, W. Yang and J. He, *Small*, 2018, **14**, e1704164.
3. M. Tuchband, J. He, S. Huang and S. Lindsay, *Rev. Sci. Instrum.*, 2012, **83**, 015102.
4. S. Mahajan, T.-C. Lee, F. Biedermann, J. T. Hugall, J. J. Baumberg and O. A. Scherman, *Phys. Chem. Chem. Phys.*, 2010, **12**, 10429.
5. C. A. Tao, Q. An, W. Zhu, H. Yang, W. Li, C. Lin, D. Xu and G. Li, *Chem. Commun.*, 2011, **47**, 9867.
6. Y. Chen, A. Klimczak, E. Galoppini and J. V. Lockard, *RSC Adv.*, 2013, **3**, 1354.
7. C.-H. Chen, E. R. Ravenhill, D. Momotenko, Y.-R. Kim, S. C. S. Lai and P. R. Unwin, *Langmuir*, 2015, **31**, 11932.